Microsphere-aided Optical Microscopy and its Applications for Super-Resolution Imaging

Paul Kumar Upputuri, Manojit Pramanik*

School of Chemical and Biomedical Engineering, Nanyang Technological University, 62 Nanyang Drive, Singapore 637459

Abstract. The spatial resolution of a standard optical microscope (SOM) is limited by diffraction. In visible spectrum, SOM can provide ~200 nm resolution. To break the diffraction limit several approaches were developed including scanning near filed microscopy, metamaterial super-lenses, nanoscale solid immersion lenses, super-oscillatory lenses, confocal fluorescence microscopy, techniques that exploit non-linear response of fluorophores like stimulated emission depletion microscopy, stochastic optical reconstruction microscopy, etc. Recently, photonic nanojet generated by a dielectric microsphere was used to break the diffraction limit. The microsphere-approach is simple, cost-effective and can be implemented under a standard microscope, hence it has gained enormous attention for super-resolution imaging. In this article, we briefly review the microsphere approach and its applications for super-resolution imaging in various optical imaging modalities.

Keywords: Super-resolution, microsphere, photonic nanojet, optical nanoscopy.

Address all correspondence to: Manojit Pramanik, Nanyang Technological University, School of Chemical and Biomedical Engineering, 62 Nanyang Drive, Singapore 637459; Tel: +65-6790-5835; Fax: +65-6791-1761; E-mail: manojit@ntu.edu.sg

1. Introduction

Optical or light microscopy is one of the most significant scientific achievements in the history of science. Optical microscopy employs visible light to detect/image microscale objects. It is a well-known and well-used tool for optical imaging [1, 2] and optical metrology [3-6] applications. However, the far-field imaging resolution of any microscope is limited by the diffraction of optical waves. Some methods that exploit non-linear response of fluorophores like stimulated emission depletion microscopy (STED) [7], stochastic optical reconstruction microscopy (STORM) [8] bypass the diffraction limit of light microscopy to increase resolution. The diffraction limit is $d \approx 0.61\lambda/NA$ according to Rayleigh criterion, where λ is the free-space light wavelength, and NA is the numerical aperture. A standard microscope has a resolution limit of around half the wavelength ($\sim\lambda/2$). In the recent years, numerous efforts have been attempted to overcome this diffraction limit and achieve super-resolution imaging. There are commercially available non-optical microscopes including Atomic force microscopy (AFM), Magnetic force microscopy (MFM), Scanning electron microscopy (SEM), and Transmission electron microscopy (TEM) etc., which can provide lateral resolution ~30 nm, ~20 nm, ~1 nm to 20 nm, and ~0.1 nm, respectively. These techniques are expensive, and may also require sample preparation. Optical methods to achieve super-resolution can be classified into several types: scanning near filed optical microscopy (SNOM) [9], utilizing non-linear effects of fluorophores (STED [7], STORM [8]), increasing object-space refractive index (solid immersion lens (SIL) [10, 11]), using aspheric mirror to increase angle (parabolic mirror [12], elliptical mirror [13]), pupil filtering methods (super-oscillatory lenses [14]); aperture synthesis (structured illumination microscopy (SIM) [15], Fourier ptychographic microscopy (FPM) [16]), microscopy with near field structures assisted (microsphere, micro-droplets, micro-fiber). In the SIL technique, the resolution is improved due

to an increase in the numerical aperture of the imaging system, $NA = nsin\theta$, where n is the object-space refractive index and θ is the half-angle of the objective acceptance cone. It has also been demonstrated that the diffraction limit can be exceeded by using micro- and nano-SILs [11]. However, such lenses are challenging to fabricate.

A far-field sub-diffraction-limited imaging was demonstrated by super-oscillatory lenses. The lateral resolution achieved with the super-oscillatory lens was around $(\sim\lambda/6)$ $(i.e., 105\ nm)$ [14]. Several alternative ways to break the diffraction limit have been reported including nanoscale solid immersion lenses (n-SIL) [17], micro-droplets [18], and micro-fiber [19] etc. The lateral resolutions achieved with these approaches were $(\sim\lambda/4)$ $(i.e., 126\ nm), (\sim\lambda/8)$ $(i.e., 60\ nm), (\sim\lambda/8)$ $(i.e., 70\ nm)$, respectively.

More recently, a white light microscope with glass microspheres in air medium was demonstrated [20]. With $2-9\ um$ glass sphere (refractive index $n1\sim1.46$, a lateral resolution $\sim50\ nm$ $(\sim\lambda/8)$ was achieved. The super-resolution is due to "photonic nanojet" (PNJ) generated by the microsphere. When microsphere is illuminated by a light waves, a narrow (less than$\sim\lambda/2$), strong, low-diverging, non-evanescent and jet like beam is generated on the shadow side of the microsphere [21, 22]. Such jet like beam can break the diffraction limit in optical microscopy by reducing the size of the excitation volume. The signal generated in the excitation volume can still be collected in the far-field. The influence of the sphere and its design on the properties of nanojet including width, length, working distance, peak intensity was reported in Ref. [23]. The factors that can influence the PNJ properties are sphere size, wavelength, sphere refractive index, medium

refractive index, numerical aperture of the objective, shape design etc. [24]. First, the microsphere approach was demonstrated with fused silica spheres $n1{\sim}1.46$ and diameters $2-9\ um$ [20]. Here the authors concluded that the use of higher-index spheres >1.8, and the use of liquid-immersion spheres are not suitable for microsphere-aided imaging. However, later it was found that the high-index microspheres $n1{\sim}1.9-2.1$ with larger diameters $50-200\ um$ totally immersed liquid could provide super-resolution imaging down to $\sim\lambda/8$ [25].

The schematic of the standard optical microscope (SOM), and microsphere-aided optical microscope (MAOM) are illustrated in Figs. 1(a) and 1(b), respectively. In MAOM, a whole sphere (with diameter $'D'$ and refractive index $n1$) is placed on the sample surface as shown in Fig. 1(b). To visualize the image the objective needs to be moved towards the sample as illustrated in Figs. 1(a) and 1(b). A virtual image is formed at a distance $D(n1-1)/(2-n1)$, underneath the sample's surface. The image magnification of the sphere calculated from the geometric optics is $n1/(2-n1)$ [10]. Label-free super-resolution imaging of $75\ nm$ viruses was demonstrated by combing submerged microsphere with standard microscopy. The magnification of $30-100\ um$ polystyrene (PS) microsphere in air was $\sim 8X$, whereas the magnification of $3\ um$ fused silica microsphere semi-immersed in ethanol was 2.0X [26]. Although, large-diameter microspheres could provide high magnification, but it is difficult to achieve beyond $50\ nm$ resolution. A micro-pipet controlled microsphere for moving and positioning was demonstrated for wide-field nanoscopy. The microsphere-approach was successfully demonstrated in other imaging modalities including fluorescence microscopy [27], Raman microscopy [28, 29], coherent anti-stokes Raman scattering microscopy [30, 31], photoacoustic microscopy [23, 24] etc. Not only for imaging, photonic nanojets were also used for lithography [32, 33], Raman signal enhancement [34],

detection/sensing of nanoparticles [35], enhancing the back scattered light [22, 36, 37], fiber-optics [38], Surface enhanced Raman scattering [28], etc. In this article, we will briefly review the microsphere nanoscope and its super-resolution imaging applications in various imaging modalities. We discuss the use of microsphere for super-resolution imaging in white light microscopy (section 2), scanning laser confocal microscopy (section 3), coherent anti-Stokes Raman Scattering microscopy (section 4), fluorescence microscopy (section 5), photoacoustic microscopy (section 6), and finally the discussions and future direction (section 7).

2. Applications of microsphere for super-resolution imaging

2.1 White light microscopy - Microsphere in air medium

Fig. 1(a) illustrates the schematic of a white-light microscope with microsphere placed on the surface of the sample [20]. A halogen lamp with a peak wavelength of $600\ nm$ was used as the excitation source. The microsphere magnifies the object to form virtual image in the far-field as shown in Fig. 1(a). The standard microscope picks it up by a conventional $80X$ objective lens (numerical aperture, $NA = 0.9$). A grating [Fig. 1(b)] with $360\ nm$-wide lines, spaced $130\ nm$-apart, was imaged using $4.75\ um$ diameter silica microspheres. The virtual image plane was $2.5\ um$ below the sample surface. From Fig. 1c, it is clear that only those lines with microsphere on top of them have been resolved. For $\lambda = 400\ nm$, the best diffraction-limited resolution was $\sim 271\ nm$ in air, so, the lines without microspheres on top were not resolved. The focal planes for lines with and without microsphere on top are different. The object was $4.17X$ times magnified in Fig. 1(c). Figure 1(d) shows a SEM image of gold-coated anodicaluminium oxide (AAO) membrane imaged with $4.75\ um$ diameter microspheres. The AAO sample had pores diameter

$\sim 50\ nm$ and spaced apart $\sim 50\ nm$. The microsphere assisted to resolve the 50 nm tiny pores that were well beyond the diffraction limit, giving a resolution of between $\lambda/8$ ($\lambda = 400\ nm$), and $\lambda/14$ ($\lambda = 750\ nm$) [Fig. 1(e)]. Figs. 1(f) and 1(g) show the SEM image and reflection mode image of a star structure made on SbTe disk, respectively. The star, including the 90 nm corners, was clearly resolved by the microsphere.

The microsphere in air medium demonstrated a far-field resolution between $(\lambda/8\ -\lambda/14)$ and magnification between $(4X - 8X)$. The theoretical calculations predicted that the super-resolution strength is maximum at $n1 \sim 1.8$. For materials with refractive index $n1 > 1.8$, the super-resolution strength reduces, making it undesirable to use such high-index materials for super-resolution imaging [20]. Later, it was demonstrated that by totally immersing high-index $n1 \sim 1.9 - 2.1$ microspheres in liquids it is possible to resolve feature of order of $\sim\lambda/7$. In the following sub-sections we will discuss the super-resolution capabilities of immersed microspheres.

2.2 White light microscopy - Microsphere in liquid medium

Super-resolution imaging was demonstrated by using fused silica microspheres in air [20]. Later it was also realized by fused silica micro-spheres with a semi-immersing liquid of ethanol [26] and microscope immersion oil [39] and a barium titanate (BaTiO3) glass microsphere immersed in isopropyl alcohol [25]. A comparative study was reported on the effect of different liquid immersion media (water, 40% sugar solution, and immersion oil) on the performance of a BaTiO3 microsphere [40]. A standard microscope with halogen lamp, $50X$ objective lens having $NA = 0.75$ was used in combination with $100\ um$ BaTiO3 glass microspheres immersed in water, 40%

sugar solution, and immersion oil as shown in Fig. 2(a). The resolution of such system was approximately 300 nm at the visible wavelengths. The SEM image of the sample (groove width $120\ nm$ and spacing $180\ nm$) is shown in Fig. 2(b). The super-resolution images of the lines magnified by the $100\ um$ BaTiO3 microsphere in three different media are shown in Figs. 2(c-e). In water and 40% sugar solution, the magnified super-resolution image was observed clearly, but image distortion was observed when oil is used it could be due to the limitation of the objective lens. The relative refractive index, image focal positions, and magnifications for the three different media are shown in Table 1. The relative refractive index is $n1/n0$, where $n0 -$ refractive index of the medium and $n1 -$ refractive index of the microsphere. From the tabulated values it is clear that the magnification and resolution depends on the relative refractive index. Optical magnification was approximately $3.3\ X$, $2.8\ X$, and $2.3\ X$ in water, $40\ \%$ sugar solution, and immersion oil, respectively. The focal planes were affected by the type of the liquid in which sphere is immersed.

2.3 White light microscopy - Microsphere in solid medium

Recently, it was demonstrated that microsphere embedded in transparent solidified film can be used for super-resolution imaging [41]. In this work, microspheres were fixed in elastomers instead of liquid. Advantages of solid-film immersion microspheres compared with liquid immersion microspheres: (i) solid-film can be pre-fabricated, (ii) solid-film can be used as cover slips, (iii) imaging can be performed by an inverted microscope, (iv) any potential influence of liquid evaporation on imaging performance can be minimized, etc.

Fig. 3(a) shows a schematic of the microsphere-embedded film placed on the sample, and an upright microscope in reflection illumination mode was used for imaging. Fig. 3(b) shows the ray diagram for the virtual image formation by the sphere. A detailed procedure for the preparation of microsphere-embedded film is discussed in Ref. [41]. The imaging object was a Verbatim blu-ray disk. Monodispersed barium titanate glass (BTG) microspheres with diameters D ~30–150 um and refractive index n ~1.9–2.1 were embedded inside the film. The films thickness was about 300 um. Imaging of the disk structure was possible through high-index BTG microspheres embedded in the polydimethylsiloxane (PDMS) layer, as shown in Figs. 3(c) and 3(d) for microspheres with $D{\sim}65\ um\ (n1{\sim}1.9)$ and $D{\sim}55\ um\ (n1{\sim}2.1)$ through a $100\ X\ (NA = 0.9)$ objective lens, respectively. It was found that the films with higher index microspheres $n1{\sim}2.1$ gave higher magnification factors and larger fields of view. However, high-index microspheres did not form an image when the immersed medium is air. But if they were immersed in liquids or elastomers, due to the relative refractive index, imaging was possible.

3. Scanning laser confocal microscopy (SLCM)

Unlike the wide-field microscopy discussed in previous sections, the SLCM [Fig. 1(a)] employs a single laser beam to scan the focusing plane in a raster pattern. The laser beam was controlled by a pair of galvanometric mirrors and focused by objective lenses on the target surface [Fig. 1(b)]. The intensity of the reflected light by the focused laser spot illumination was collected by the objective lenses and filtered by the confocal pinhole. The light passing through the pinhole comes from the focal point of the objective. Compared with conventional optical microscopes, the SLCM imaging was based on reflecting light intensity from an illuminated point rather than a wide-field projection [42]. Figs. 4(a) and 4(b) show the schematic of the experimental configuration and

optical path for microsphere-coupled Scanning laser confocal microscopy (mSLCM). Two different The microspheres used here were made out of fused silica (FS) $n1 = 1.47@408\ nm$ with diameters of $2.5\ um, 5.0\ um, 7.5\ um$. The SEM image of the sample gold quintuplet nanodots is shown in Fig. 4(c). As can be seen in Fig. 4(d), the standard SLCM without microsphere coupling cannot distinguish the gold quintuplet nanodots with $25\ nm\ (\lambda/17)$ separations of peripheral dots to the central one. However, the nanodots can be nearly resolved by the $5\ um -$ diameter fused silica mSLCM, as shown in Fig. 4(e). In this image, the resolved nanodots were in contact with the microsphere and it is clear, whereas the rest was distorted and blurred due to the curvature of the sphere. The experimental results indicated that the individual objects with subwavelength spatial separations can be nearly resolved by the mSLCM.

4. Coherent anti-Stokes Raman Scattering (CARS) microscopy

Coherent anti-Stokes Raman Scattering (CARS) microscopy is an advanced vibrational imaging technique [43-46]. CARS is a third-order nonlinear process where a pump beam ω_p and a Stokes beam ω_s interact through $\chi^{(3)}$ of a sample to generate an anti-Stokes beam at a frequency $\omega_{as} = 2\omega_p - \omega_s$. CARS microscopy has been used for the characterization of a wide range of biological systems [44, 47-49] and materials [50, 51]. However, like most other optical imaging techniques, its spatial resolution is limited by diffraction. For laser-scanning CARS microscopy with a pump wavelength λ_p, the lateral FWHM of the excitation volume can reach below $0.4\lambda_p$, but the lateral resolution is $0.5\lambda_p$ [52]. Various techniques including depleting CARS radiation at the periphery of the focal spot [53], structured illumination [54], and near-field scanning with an aperture [55]. A spatial resolution of $60\ nm$ or $\lambda_p/12$ with Tip-enhanced broad band (TE-BB) CARS [51, 56],

and $\sim 0.36\lambda_p$ was achieved with switching laser mode (SLAM) CARS microscopy [57]. Recently, a far-field super-resolution CARS microscopy by using photonic nanojets generated by microspheres was demonstrated [30, 31]. This method requires no modification of the optical setup, and could be very useful for the vibrational imaging of films or surfaces.

The epi-CARS (E-CARS) microscope is shown in Fig. 5(a) [30]. The laser source used was Orpheus-Twin OPAs pumped by Pharos-9W (220 fs, 1028 nm, 1 MHz). The twin OPAs can generate 120 fs pulses in 630-2600 nm range. The 1028 nm Stokes beam and 726 nm pump beam from OPA, resulting in a Raman shift $\omega_p - \omega_s$ at 2840 cm^{-1}. These beams were sent into an inverted laser-scanning microscope (Nikon Ti-Eclipse), and were focused into the sample by a 60X 1.0-NA water objective (MO-W). The average pump and Stokes laser power before the objective were 0.3 mW each. The CARS signal was separated from the laser beams by a 650 nm short-pass dichroic mirror (DM), filtered with a 650/60 nm band-pass filter, and then detected by a photomultiplier tube (PMT). The images were acquired at 1 frame/sec, and scanning area was 40 um x 40 um. The diffraction-limited resolution of the E-CARS microscope was about 400 nm. The imaging targets were sub-diffraction features on an organic azo-dye film. The film has 200 nm wide stripes separated by 100 nm wide and 20 nm deep grooves. The film was imaged at the Raman shift of 2840 cm^{-1}, for which the CARS wavelength was 649 nm.

The sample with microspheres on its surface was placed on the microscope with the film layer facing down as in Fig. 5(a). CARS images were collected at various focal planes by moving the objective. Images obtained on a sample having 1-4 um spheres are shown in Figs. 5(b) and 5(c).

Fig. 5(b) was acquired when the focal plane was on the sample, and hence strong CARS signal was observed everywhere. Outside the microspheres, the E-CARS microscope could not resolve the sub-diffraction patterns on the film (100-nm grooves and 200-nm stripes) due the diffraction-limited resolution. But, the spheres aided to resolve the sub-diffraction patterns in their viewing window. The stripes had more matter than the grooves, and therefore stripes produced higher CARS signal than the grooves when nanojets scanned across them. Thus, the bright parallel lines in Figs. 5(b) and 5(c) are the images of the stripes. Fig. 5(d) shows the comparison of the intensity profiles along the line indicated in Figs. 5(b and c). It was demonstrated that super-resolution CARS imaging with nanojets generated by SiO2 microspheres is possible. A virtual magnification up to 5.0X and a far-field lateral resolution of at least $\lambda_p/4$ at 796 nm pump laser wavelength were observed.

5. Fluorescent microscopy

A standard fluorescent microscopy combined with transparent barium titanate glass microspheres was demonstrated for super-resolution imaging [27]. The microscope has NA 0.8, 40X water immersion objective and NA 1.4, 63X oil immersion objective. The microspheres were immersed in liquid medium with refractive index (1.33 for water, or 1.52 for oil). For fluorescence imaging, a mercury lamp and the water immersion objective were used. Figure 6(a) and 6(b) show the imaging of polystyrene fluorescent particles with emission wavelength 680 nm. A 1 um-diameter particle [Fig. 6(a)] was 5.4 times magnified [Fig. 6(b)] by using a barium titanate microsphere with diameter of 60 um. The diffraction-limited resolution of water-immersion objective at a fluorescent emission wavelength of 680 nm is 404 nm. 100 nm-diameter particles were dispersed on a glass substrate, which cannot be resolved through standard fluorescent microscopy [Fig. 6(c)]. These

particles were clearly imaged through the microsphere in Fig. 6(d). Thus using a 60 um barium titanate microsphere a resolution $\sim\lambda/7$ was demonstrated in fluorescence microscopy.

6. Photoacoustic microscopy

Along with pure optical methods discussed in the previous sections, microsphere approach seems to be feasible for achieving super-resolution in photoacoustic imaging (PAI) [23, 24]. PAI is an emerging hybrid imaging modality for both preclinical and clinical applications [58-63]. In PAT, nanosecond laser pulses irradiate the sample (biological tissue). The absorption of light by the tissue chromophores leads to local temperature rise, which then yields pressure waves emitted in the form of sound waves. An ultrasound detector collects the photoacoustic signals at various positions around the sample (biological tissue). The photoacoustic signals are used to generate images of the internal structure and function of the biological tissue. Optical resolution photoacoustic microscopy (ORPAM) is a high-resolution version of the photoacoustic imaging systems [59, 62, 64]. ORPAM has several advantages over pure optical methods: (a) ORPAM makes use of the weak acoustic scattering to do high resolution imaging beyond the optical diffusion limit (~1 mm), (b) it is highly scalable 3D *in vivo* imaging modality, both imaging depth and resolution are scalable, (c) it provides optical absorption contrast unlike confocal fluorescence microscopy and optical coherence tomography (OCT) which provide fluorescence and scattering contrast, (d) it directly images optical absorption with 100% relative sensitivity and the sensitivity is two orders of magnitude greater than those of confocal microscopy and optical coherence tomography (OCT) [63], (e) it can simultaneously image functional, structural, molecular, flow dynamic and metabolic contrasts *in vivo* [63, 65-67].

In ORPAM the optical focus is finer, than the acoustic focus. So, the size of optical spot (function of wavelength, and numerical aperture) limits the imaging resolution in ORPAM. ORPAM systems with resolution 5 um using NA = 0.1 and λ = 590 nm [68], 2 um using NA = 0.47 and λ = 532 nm [69], and 0.22 um using NA = 1.23 and λ = 532 nm [70] were demonstrated. Using UV light, *in vivo* label-free PAM of cell nuclei by excitation of DNA and RNA was demonstrated [71]. 10-nm gold nanoparticles were imaging using a nonlinear super-resolution photoacoustic microscopy [72]. A label-free photoacoustic nanoscopy using optical saturation and polynomial fitting was demonstrated for imaging mitochondria in NIH 3T3 fibroblasts [73]. A photoimprint PAM using double-excitation process was demonstrated for sub-diffraction limited lateral resolution [74]. These approaches are either complicated or expensive or both.

A simulation study was reported on achieving super-resolution in ORPAM using photonic nanojets [24]. The important parameters of PNJ [described in Fig. (7)] including Fp-focal length, Wp-full width at half maximum, Lp-effective length, Ip-peak intensity of photonic nanojet were studied. It was shown that the sphere size (D), wavelength (λ), sphere refractive index (n1), medium refractive index (n0), numerical aperture (NA) of the objective, will affect the PNJ parameters. Fig. 8 shows the influence of incident wavelength on the focused Gaussian beam and photonic nanojet [24]. It was shown that the PNJ parameters can be controlled by changing the sphere design. The performance of different sphere designs including Round microsphere (RM), Truncated Microsphere (TM) [75], Microsphere with Concentric Rings (MCR) [76], Multi-Layer Microsphere (MLM) [77, 78], etc. was compared in Ref. [23].

The properties, such as the effective length (L_p), and full width half maximum (W_p), focal length (F_p), peak intensity (I_p) of the photonic nanojets generated when a 5 μm sphere was placed inside a focusing Gaussian beam with 3958 nm waist size, are listed in the Table 1. The brief summary of the table is: (i) FWHM widths of all the photonic nanojets (W_p) are smaller than the Gaussian focus (*i.e.*, W_g = 3958 nm). (ii) Increase in 'n1' will reduce the PNJ width, length, and working distance. The PNJ is elongated at the expense of PNJ broadenig and intensity lowering. (iii) Round microsphere (RM) design could generate strong and narrow nanojet. But the drawback with the RM design is it could only generate nanojet with short length and short working ditance (~10λ). (iv) By simply cutting the round sphere, the PNJ can be was elongated, (v) In case of MCR design, the number of rings (2, 3, or 4) made on the round silica sphere does not infulence the PNJ parameters much. However, the length and working distance are slightly better compared to the RM silica sphere (n1 = 1.45). (vi) By proporly selecting the sphere and layer materials, the two-layer design is promising to generate ultra-long nanojet. With n1 = 1.51 and n2 = 1.38, ~40 um-long nanojet was generated. (vii) The TMLM design with cutting thikness, T = 0.75D = 3.75 um, showed PNJ with a remarkable extention of ~108 um (~135λ, it is the longest nanojet reported so far) and long working distance ~26 um (~32λ, it is the longest micropshere focal reported so far).

Super-resolution imaging was compared on a numerical phantom described in Fig. 9(a). It was scanned by the photonic nanojet shown in Fig. 8(d). Fig. 9(b) shows the 2D B-scan PAM images of the target excited with photonic nanojets with FWHM ~208 nm [Fig. 8(d)]. The images shown in Fig. 9(b) ware acquired using 375 MHz UST. The smaller gap of 200 nm between the two square target objects was resolved. Fig. 9(c) shows the normalized profile along the line indicated on Fig. 9(b). The targets are resolved, demonstrating the ability of breaking through the diffraction-

limited lateral resolution in ORPAM with the help of photonic nanojets to achieve super-resolution. The COMSOL simulations for Gaussian beam/photonic nanojet, and k-wave simulations for generating super-resolution photoacoustic B-scan images are disused in detail in Ref. [23, 24].

7. Discussion and future directions

The optics of photonic nanojets proved that it can break the diffraction limit [21, 22, 37, 79]. The photonic nanojets from microspheres were directly imaged [80]. The resolution capabilities of microsphere were proved under different imaging microscopy systems as discussed here. White light microscopy combined (i) with low- refractive index fused silica microsphere in air demonstrated a far-field resolution ~50 nm ($\lambda/8 - \lambda/14$), (ii) with high-refractive index barium titanate (BaTiO3) microsphere in liquid demonstrated a resolution ~($\lambda/7$), (iii) with high-refractive index BaTiO3 microsphere in solid polydimethylsiloxane (PDMS) film demonstrated a resolution ~($\lambda/7$). Scanning laser confocal microscopy (SLCM) combined with fused silica microsphere in air demonstrated a resolution about 25 nm ($\lambda/17$) . CARS microscopy combined with fused silica sphere in air showed a virtual magnification up to 5.0X and a far-field lateral resolution ~$\lambda/4$ at 796 nm pump laser wavelength. Using 60 um barium titanate microsphere a resolution ~$\lambda/7$ was demonstrated in fluorescence microscopy with water immersion objective. In photoacoustic microscopy, through simulation, it was shown that ~$\lambda/4$ *i.e.*, ~200 nm resolution is possible to achieve using fused silica spheres. Very recently, the unusual properties of nanojets [81], and the influence of background media on super-resolution imaging were studied in Ref. [82]. The microsphere-approach is robust, economical and can be implemented under a standard

microscope for imaging objects where nanoscale resolution is required. Although, microsphere approach proved its potential for super-resolution imaging, this approach is still under developing stage.

In future, research work needs to be progressed to make improvements in this approach. Microsphere design that can provide nanojet with high Q-factor $\left(Q = [\frac{Lp}{Wp}]Ip\right)$ [23] and long working distance is required. By embedding the sphere in polydimethylsiloxane (PDMS), photopolymers, or epoxies, it might be possible to fabricate thin films containing high-index microspheres made from BTG or chalcogenide glasses, titanium, zirconium or zinc oxides, or silicon. Such thin films can be used as contact optical components to enhance the resolution capability of standard microscopes. Compared to whole sphere, truncated sphere can generate long PNJ with long working distance which is desirable for non-contact imaging. With a sphere in air medium, maximal virtual image magnification can be obtained with refractive index $n1 = 1.8$. With 5 μm sphere ($n1 = 1.8$), it should resolve arbitrary structures $< 20\ nm$, making it possible to directly observe viruses and the inside of living cells under white light microscopy.

Acknowledgement

The authors would like to acknowledge the financial support from the Tier 1 research grant funded by the Ministry of Education in Singapore (RG48/16: M4011617), and Tier 2 research grant funded by Ministry of Education in Singapore (ARC2/15: M4020238). Authors have no relevant financial interests in the manuscript and no other potential conflicts of interest to disclose.

References

[1] W.H. De Vos, D. Beghuin, C.J. Schwarz, D.B. Jones, J.J. van Loon, J. Bereiter-Hahn, E.H. Stelzer, Invited review article: Advanced light microscopy for biological space research, Rev. Sci. Instrum., 85 (2014) 101101.

[2] A.R. Kherlopian, T. Song, Q. Duan, M.A. Neimark, M.J. Po, J.K. Gohagan, A.F. Laine, A review of imaging techniques for systems biology, BMC Syst. Biol., 2 (2008) 74.

[3] P.K. Upputuri, M. Pramanik, K.M. Nandigana, M.P. Kothiyal, Multi-colour microscopic interferometry for optical metrology and imaging applications, Optics and Lasers in Engineering, 84 (2016) 10-25.

[4] P.K. Upputuri, L. Gong, H. Wang, M. Pramanik, K.M. Nandigana, M.P. Kothiyal, Measurement of large discontinuities using single white light interferogram, Opt. Express, 22 (2014) 27373.

[5] U.P. Kumar, W. Haifeng, N.K. Mohan, M.P. Kothiyal, White light interferometry for surface profiling with a colour CCD, Optics and Lasers in Engineering, 50 (2012) 1084-1088.

[6] U.P. Kumar, B. Bhaduri, M.P. Kothiyal, N.K. Mohan, Two-wavelength micro-interferometry for 3-D surface profiling, Optics and Lasers in Engineering, 47 (2009) 223-229.

[7] Javad N. Farahani, Matthew J. Schibler, L.A. Bentolila, Stimulated emission depletion (STED) microscopy: from theory to practice, Formatex Research Center, Spain, 2010.

[8] M.J. Rust, M. Bates, X. Zhuang, Sub-diffraction-limit imaging by stochastic optical reconstruction microscopy (STORM), Nat Methods, 3 (2006) 793-795.

[9] U. Dürig, D.W. Pohl, F. Rohner, Near-field optical-scanning microscopy, J. Appl. Phys., 59 (1986) 3318-3327.

[10] A. Darafsheh, N.I. Limberopoulos, J.S. Derov, D.E. Walker, V.N. Astratov, Advantages of microsphere-assisted super-resolution imaging technique over solid immersion lens and confocal microscopies, Appl Phys Lett, 104 (2014) 061117.

[11] D.R. Mason, M.V. Jouravlev, K.S. Kim, Enhanced resolution beyond the Abbe diffraction limit with wavelength-scale solid immersion lenses, Opt. Lett., 35 (2010) 2007-2009.

[12] J. Stadler, C. Stanciu, C. Stupperich, A.J. Meixner, Tighter focusing with a parabolic mirror, Opt. Lett., 33 (2008) 681-683.

[13] J. Liu, M. Ai, H. Zhang, J. Tan, Focusing properties of elliptical mirror with an aperture angle greater than π, Optics Engineering, 53 (2014) 061606.

[14] E.T. Rogers, J. Lindberg, T. Roy, S. Savo, J.E. Chad, M.R. Dennis, N.I. Zheludev, A super-oscillatory lens optical microscope for subwavelength imaging, Nature materials, 11 (2012) 432-435.

[15] L. Shao, P. Kner, E.H. Rego, M.G. Gustafsson, Super-resolution 3D microscopy of live whole cells using structured illumination, Nat Methods, 8 (2011) 1044-1046.

[16] G. Zheng, R. Horstmeyer, C. Yang, Wide-field, high-resolution Fourier ptychographic microscopy, Nat Photonics, 7 (2013) 739-745.

[17] J.Y. Lee, B.H. Hong, W.Y. Kim, S.K. Min, Y. Kim, M.V. Jouravlev, R. Bose, K.S. Kim, I.-C. Hwang, L.J. Kaufman, C.W. Wong, P. Kim, K.S. Kim, Near-field focusing and magnification through self-assembled nanoscale spherical lenses, Nature, 460 (2009) 498-501.

[18] Smolyaninova, V. N., I.I. Smolyaninov, A.V. Kildishev, V.M. Shalaev, Maxwell fish-eye and Eaton lenses emulated by microdroplets, Opt. Lett., 35 (2010) 3396-3398.

[19] X. Hao, X. Liu, C. Kuang, Y. Li, Y. Ku, H. Zhang, H. Li, L. Tong, Far-field super-resolution imaging using near-field illumination by micro-fiber, Appl Phys Lett, 102 (2013) 013104.

[20] Z. Wang, W. Guo, L. Li, B. Luk'yanchuk, A. Khan, Z. Liu, Z. Chen, M. Hong, Optical virtual imaging at 50 nm lateral resolution with a white-light nanoscope, Nature communications, 2 (2011) 218.

[21] A.V. Itagi, W.A. Challener, Optics of photonic nanojets, Journal of Optical Scociety of America A, 22 (2005) 2847.

[22] Z. Chen, A. Taflove, V. Backman, Photonic nanojet enhancement of backscattering of light by nanoparticles: a potential novel visible-light ultramicroscopy technique, Opt. Express, 12 (2004) 1214-1220.

[23] P.K. Upputuri, M. Krishnan, M. Pramanik, Microsphere enabled sub-diffraction limited optical-resolution photoacoustic microscopy: a simulation study, J. Biomed. Opt., 22 (2017) 045001.

[24] P.K. Upputuri, Z.-B. Wen, Z. Wu, M. Pramanik, Super-resolution photoacoustic microscopy using photonic nanojets: a simulation study, J. Biomed. Opt., 19 (2014) 116003.

[25] A. Darafsheh, G.F. Walsh, L.D. Negro, V.N. Astratov, Optical super-resolution by high-index liquid-immersed microspheres, Appl Phys Lett, 101 (2012) 141128.

[26] X. Hao, C. Kuang, X. Liu, H. Zhang, Y. Li, Microsphere based microscope with optical super-resolution capability, Appl Phys Lett, 99 (2011) 203102.

[27] H. Yang, N. Moullan, J. Auwerx, M.A.M. Gijs, Super-resolution biological microscopy using virtual imaging by a microsphere nanoscope, Small, 10 (2014) 1712-1718.

[28] G.M. Das, R. Laha, V.R. Dantham, Photonic nanojet-mediated SERS technique for enhancing the Raman scattering of a few molecules, J. Raman Spectrosc., 47 (2016) 895-900.

[29] J. Kasim, T. Yu, Y.Y. Meng, L.J. Ping, A. See, L.L. Jong, S.Z. Xiang, Near-field Raman Imaging using Optically Trapped Dielectric Microsphere, Opt. Express, 16 (2008) 7976-7984.

[30] P.K. Upputuri, Z. Wu, L. Gong, C.K. Ong, H. Wang, Super-resolution coherent anti-Stokes Raman scattering microscopy with photonic nanojets, Opt. Express, 22 (2014) 12890-12899.

[31] X. Huang, X.N. He, W. Xiong, Y. Gao, L.J. Jiang, L. Liu, Y.S. Zhou, L. Jiang, J.F. Silvain, Y.F. Lu, Contrast enhancement using silica microspheres in coherent anti-Stokes Raman spectroscopic imaging, Opt. Express, 22 (2014) 2889-2896.

[32] A. Bonakdar, M. Rezaei, R.L. Brown, V. Fathipour, E. Dexheimer, S.J. Jang, H. Mohseni, Deep-UV microsphere projection lithography, Opt. Lett., 40 (2015) 2537-2540.

[33] W. Wu, A. Katsnelson, O.G. Memis, H. Mohseni, A deep sub-wavelength process for the formation of highly uniform arrays of nanoholes and nanopillars, Nanotechnology, 18 (2007) 485302.

[34] V.R. Dantham, P.B. Bisht, C.K.R. Namboodiri, Enhancement of Raman scattering by two orders of magnitude using photonic nanojet of a microsphere, J. Appl. Phys., 109 (2011) 103103.

[35] H. Yang, M. Cornaglia, M.A. Gijs, Photonic nanojet array for fast detection of single nanoparticles in a flow, Nano Lett., 15 (2015) 1730-1735.

[36] M.-S. Kim, T. Schart, S. Mühligb, C. Rockstuhlb, H.P. Herzig, Photonic Nanojet engineering: Focal point shaping with scattering phenomena of dielectric microspheres, Proc Spie2011, pp. 794115.

[37] X. Li, Z. Chen, A. Taflove, V. Backman, Optical analysis of nanoparticles via enhanced backscattering facilitated by 3-D photonic nanojets, Opt. Express, 13 (2005) 526-533.

[38] V.N. Astratov, A. Darafsheh, M.D. Kerr, K.W. Allen, N.M. Fried, A.N. Antoszyk, H.S. Ying, Photonic nanojets for laser surgery, SPIE Newsroom, (2010).

[39] X. Hao, C. Kuang, Y. Li, X. Liu, Y. Ku, Y. Jiang, Hydrophilic microsphere based mesoscopic-lens microscope (MMM), Opt. Commun., 285 (2012) 4130-4133.

[40] S. Lee, L. Li, Z. Wang, W. Guo, Y. Yan, T. Wang, Immersed transparent microsphere magnifying sub-diffraction-limited objects, Appl. Opt., 52 (2013) 7265-7270.

[41] A. Darafsheh, C. Guardiola, A. Palovcak, J.C. Finlay, A. Cárabe, Optical super-resolution imaging by high-index microspheres embedded in elastomers, Opt. Lett., 40 (2014) 5.

[42] Yinzhou Yan, Lin Li, Chao Feng, Wei Guo, Seoungjun Lee, M. Hong, Microsphere-coupled scanning laser confocal nanoscope for sub-diffraction-limited Imaging at 25 nm lateral resolution in the visible spectrum, Acs Nano, 8 (2014) 1809–1816.

[43] P.K. Upputuri, L. Gong, H. Wang, Chirped time-resolved CARS microscopy with square-pulse excitation, Opt. Express, 22 (2014) 9611-9626.

[44] P.K. Upputuri, J. Lin, L. Gong, X. Liu, H. Wang, Z. Huang, Circularly polarized coherent anti-Stokes Raman scattering microscopy, Opt. Lett., 38 (2013) 1262-1264.

[45] P.K. Upputuri, H. Wang, A picosecond near-infrared laser source based on a self-seeded optical parametric generator, Applied Physics B, 112 (2013) 521-527.

[46] J.X. Cheng, X.S. Xie, Coherent anti-Stokes Raman scattering microscopy: Instrumentation, theory, and applications, Journal of Physical Chemistry B, 108 (2004) 827-840.

[47] Y. Fu, T.B. Huff, H.W. Wang, H.F. Wang, J.X. Cheng, Ex vivo and in vivo imaging of myelin fibers in mouse brain by coherent anti-Stokes Raman scattering microscopy, Opt. Express, 16 (2008) 19396-19409.

[48] H.F. Wang, Y. Fu, P. Zickmund, R.Y. Shi, J.X. Cheng, Coherent anti-stokes Raman scattering imaging of axonal myelin in live spinal tissues, Biophys. J., 89 (2005) 581-591.

[49] A. Volkmer, J.X. Cheng, X.S. Xie, Vibrational imaging with high sensitivity via epidetected coherent anti-Stokes Raman scattering microscopy, Phys. Rev. Lett., 87 (2001).

[50] J. Lin, K. Zi Jian Er, W. Zheng, Z. Huang, Radially polarized tip-enhanced near-field coherent anti-Stokes Raman scattering microscopy for vibrational nano-imaging, Appl Phys Lett, 103 (2013) 083705.

[51] T. Ichimura, N. Hayazawa, M. Hashimoto, Y. Inouye, S. Kawata, Tip-enhanced coherent anti-Stokes Raman scattering for vibrational nanoimaging, Phys. Rev. Lett., 92 (2004).

[52] J.X. Cheng, A. Volker, X.S. Xie, Theoretical and experimental characterization of coherent anti-Stokes Raman scattering microscopy, JOSA B, 19 (2002) 1363-1375.

[53] W.P. Beeker, P. Gross, C.J. Lee, C. Cleff, H.L. Offerhaus, C. Fallnich, J.L. Herek, K.J. Boller, A route to sub-diffraction-limited CARS Microscopy, Opt. Express, 17 (2009) 22632-22638.

[54] I. Toytman, D. Simanovskii, D. Palanker, On illumination schemes for wide-field CARS microscopy, Opt. Express, 17 (2009) 7339-7347.

[55] R.D. Schaller, J. Ziegelbauer, L.F. Lee, L.H. Haber, R.J. Saykally, Chemically selective imaging of subcellular structure in human hepatocytes with coherent anti-stokes Raman scattering (CARS) near-field scanning optical microscopy (NSOM), Journal of Physical Chemistry B, 106 (2002) 8489-8492.

[56] K. Furusawa, N. Hayazawa, F.C. Catalan, T. Okamoto, S. Kawata, Tip-enhanced broadband CARS spectroscopy and imaging using a photonic crystal fiber based broadband light source, J. Raman Spectrosc., 43 (2012) 656-661.

[57] A. Gasecka, A. Daradich, H. Dehez, M. Piché, D. Côté, Resolution and contrast enhancement in coherent anti-Stokes Raman-scattering microscopy, Opt. Lett., 38 (2013) 4510.

[58] P.K. Upputuri, M. Pramanik, Recent advances toward preclinical and clinical translation of photoacoustic tomography: a review, J. Biomed. Opt., 22 (2017) 041006.

[59] L. Lin, J. Yao, R. Zhang, C.C. Chen, C.H. Huang, Y. Li, L. Wang, W. Chapman, J. Zou, L.V. Wang, High-speed photoacoustic microscopy of mouse cortical microhemodynamics, Journal of biophotonics, (2016).

[60] L.V. Wang, J. Yao, A practical guide to photoacoustic tomography in the life sciences, Nat Methods, 13 (2016) 627-638.

[61] P.K. Upputuri, K. Sivasubramanian, C.S.K. Mark, M. Pramanik, Recent Developments in Vascular Imaging Techniques in Tissue Engineering and Regenerative Medicine, BioMed Research International, 2015 (2015) 9.

[62] J. Yao, L. Wang, J.M. Yang, K.I. Maslov, T.T.W. Wong, L. Li, C.H. Huang, J. Zou, L.V. Wang, High-speed label-free functional photoacoustic microscopy of mouse brain in action, Nat Methods, 12 (2015) 407-410.

[63] L.V. Wang, S. Hu, Photoacoustic Tomography: In Vivo Imaging from Organelles to Organs, Science, 335 (2012) 1458-1462.

[64] M. Moothanchery, M. Pramanik, Performance Characterization of a Switchable Acoustic and Optical Resolution Photoacoustic Microscopy System, Sensors, 17 (2017) 357.

[65] C. Xie, P.K. Upputuri, X. Zhen, M. Pramanik, K. Pu, Self-Quenched Semiconducting Polymer Nanoparticles for Amplified In Vivo Photoacoustic Imaging, Biomaterials, 119 (2017) 1-8.

[66] M. Schwarz, A. Buehler, J. Aguirre, V. Ntziachristos, Three-dimensional multispectral optoacoustic mesoscopy reveals melanin and blood oxygenation in human skin in vivo, Journal of biophotonics, 9 (2016) 55-60.

[67] S. Huang, P.K. Upputuri, H. Liu, M. Pramanik, M. Wang, A dual-functional benzobisthiadiazole derivative as an effective theranostic agent for near-infrared photoacoustic imaging and photothermal therapy, Journal of Materials Chemistry B, 4 (2016) 1696-1703.

[68] K. Maslov, H.F. Zhang, S. Hu, L.V. Wang, Optical-resolution photoacoustic microscopy for in vivo imaging of single capillaries, Opt. Lett., 33 (2008) 929-931.

[69] G. Ku, K. Maslov, L. Li, L.V. Wang, Photoacoustic microscopy with 2-microm transverse resolution, J. Biomed. Opt., 15 (2011) 021302.

[70] C. Zhang, K. Maslov, L.V. Wang, Subwavelength-resolution label-free photoacoustic microscopy of optical absorption in vivo, Opt. Lett., 35 (2010) 3195-3197.

[71] D.K. Yao, K. Maslov, K.K. Shung, Q. Zhou, L.V. Wang, In vivo label-free photoacoustic microscopy of cell nuclei by excitation of DNA and RNA, Opt. Lett., 35 (2010) 4139-4141.

[72] D.A. Nedosekin, E.I. Galanzha, E. Dervishi, A.S. Biris, V.P. Zharov, Super-resolution nonlinear photothermal microscopy, Small, 10 (2014) 135-142.

[73] A. Danielli, K. Maslov, A. Garcia-Uribe, A.M. Winkler, C. Li, L. Wang, Y. Chen, G.W. Dorn, 2nd, L.V. Wang, Label-free photoacoustic nanoscopy, J. Biomed. Opt., 19 (2014) 086006.

[74] J. Yao, L. Wang, C. Li, C. Zhang, L.V. Wang, Photoimprint Photoacoustic Microscopy for Three-Dimensional Label-Free Subdiffraction Imaging, Phys. Rev. Lett., 112 (2014) 014302.

[75] C.-Y. Liu, Photonic nanojet shaping of dielectric non-spherical microparticles, Physica E: Low-dimensional Systems and Nanostructures, 64 (2014) 23-28.

[76] M.X. Wu, B.J. Huang, R. Chen, Y. Yang, J.F. Wu, R. Ji, X.D. Chen, M.H. Hong, Modulation of photonic nanojets generated by microspheres decorated with concentric rings, Opt. Express, 23 (2015) 20096.

[77] G. Gu, R. Zhou, Z. Chen, H. Xu, G. Cai, Z. Cai, M. Hong, Super-long photonic nanojet generated from liquid-filled hollow microcylinder, Opt. Lett., 40 (2015) 625-628.

[78] Y. Shen, L.V. Wang, J.T. Shen, Ultralong photonic nanojet formed by a two-layer dielectric microsphere, Opt. Lett., 39 (2014) 4120-4123.

[79] A. Heifetz, S.C. Kong, A.V. Sahakian, A. Taflove, V. Backman, Photonic Nanojets, Journal of Computational and Theoritical Nanoscience, 6 (2009) 1979-1992.

[80] P. Ferrand, J. Wenger, A. Devilez, M. Pianta, B. Stout, N. Bonod, E. Popov, H. Rigneault, Direct imaging of photonic nanojets, Opt. Express, 16 (2008) 6930-6940.

[81] P.Y. Li, Y. Tsao, Y.J. Liu, Z.X. Lou, W.L. Lee, S.W. Chu, C.W. Chang, Unusual imaging properties of superresolution microspheres, Opt. Express, 24 (2016) 16479-16486.

[82] A. Darafsheh, Influence of the background medium on imaging performance of microsphere-assisted super-resolution microscopy, Opt. Lett., 42 (2017) 735-738.

Captions:

Table 1 Experimentally measured magnifications and image plane positions in different media. Refractive index of BaTiO3 sphere in air is 1.9. Reproduced with permission from Ref. [40].

	Water	40% sugar solution	Microscope Immersion oil
Refractive index	1.33	1.399	1.518
Relative refractive index with BaTiO3	1.429	1.357	1.252
Magnification	3.3-3.8	2.5-3.0	2.0-2.5
One pitch size	1000 nm	850 nm	700 nm
Groove sizes	600 μm/400 μm	500 μm/350 μm	450 μm/250 μm
Focal image position	100 μm below	62 μm below	25 μm below
Focal image range	70 – 150 μm	42-87 μm	15-45 μm

Table 2 Properties of photonic nanojet generated by microspheres (with diameter, d = 5 μm) of different design when illuminated with a focusing Gaussian beam (generated in water with NA = 0.1, and λ = 800 nm) in water medium (n0 = 1.33). The FWHM waist diameter of Gaussian focus in water, Wg = 3958 nm. The highlighted ones are the best values observed in our simulations. N-number of concentric rings. *The photonic nanojets used for demonstrating photoacoustic imaging in k-wave simulations. Where Lp is the effective length, Wp is the FWHM width, Fp is the focal length of the microsphere, Ip is the peak intensity. Reproduced with permission from Ref. [23].

Design Code	Design of the Sphere	Optical and Geometric Parameters of the Sphere		PNJ Parameters			
				Lp (nm)	Wp (nm)	Fp (nm)	Ip (v^2/m^2)
RM	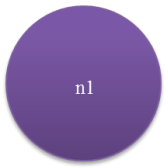	n1 = 1.45		9759*	809	5540	2.39
		n1 = 1.58		3340	500	2240	3.64
		n1 = 2.20		800	390	200	3.78
TM	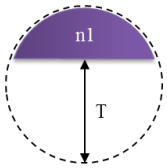	n1 = 1.45	T = 0.25D = 1.25 um	17639	1059	8709	1.99
			T = 0.50D = 2.50 um	35237	1339	11479	1.45
			T = 0.75D = 3.75 um	91633	1918	11429	1.04
MCR	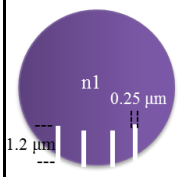	n1 = 1.45	N = 2	11839	921	6519	2.07
			N = 3	11719	899	6200	2.27
			N = 4	11199	823	5360	2.36
MLM	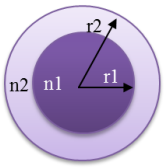	r1 = 2.4 um, r2 = 2.5 um	n1 = 1.45, n2 = 1.51	4860	603	3360	3.07
			n1 = 1.51, n2 = 1.38	40297	1538	13719	1.43
			n1 = 1.83, n2 = 1.60	3320	527	2340	2.86
TMLM		n1 = 1.45, n2 = 1.51, r1 = 2.4 um, r2 = 2.5 um	T = 0.25D = 1.25 um	8299	779	6449	2.29
			T= 0.50D = 2.50 um	17219	1020	8759	1.91

	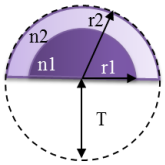		T = 0.75D = 3.75 um	66715*	1459	9629	1.34
		n1 = 1.51, n2 = 1.38, r1 = 2.4 um, r2 = 2.5 um	T = 0.25D = 1.25 um	66715	1938	19588	1.21
			T = 0.50D = 2.50 um	87033	2777	32897	1.02
			T = 0.75D = 3.75 um	107701	2977	25808	0.85
		n1 = 1.83, n2 = 1.60, r1 = 2.4 um, r2 = 2.5 um	T = 0.25D = 1.25 um	5080	667	4569	2.60
			T = 0.50D = 2.50 um	7959	779	6599	2.43
			T = 0.75D = 3.75 um	22298	1039	7349	1.63

Figure Captions:

Fig. 1. Schematic of the (a) standard optical microscope (SOM), (b) microsphere-aided optical microscope (MAOM). In MAOM, the objective needs to be moved towards the sample to capture the virtual image. The sphere forms virtual images that can be captured by the standard microscope. Microsphere imaging in transmission mode: (c) SEM image of 360-nm-wide lines spaced 130 nm apart, (d) the corresponding MAOM image shows that the lines are clearly resolved. (e) SEM image of a gold-coated AAO sample. (f) The MAOM clearly resolves the pores that are 50 nm in diameter and spaced 50 nm apart. The size of the optical image between the pores within the image plane is 400 nm. It corresponds to a magnification of 8 X. Microsphere imaging in reflection mode: (g) SEM image of a star structure made on GeSbTe thin film, (h) the complex shape of the star including 90 nm corner was clearly imaged using MAOM. A SiO2 sphere with diameter 4.74 um is used for imaging. Reproduced with permission from Ref. [20].

Fig. 2. Schematic of the microsphere optical nanoscopy in the reflective mode. (b) Scanning electron microscope (SEM) image of a film with a line width of 120 nm and a spacing of 180 nm. The magnified images through the MAOM in (b) water, (c) 40% sugar solution, and (d) microscope immersion oil using a 100 um diameter BaTiO3 microsphere. Reproduced with permission from Ref. [40].

Fig. 3. Schematic of the microsphere-assisted imaging setup in which a microsphere embedded in a PDMS film: (b) ray diagram for the virtual image formation by the sphere. The structure consisting of 200-nm stripes separated by 100-nm gaps is resolved by using the microsphere-

embedded film through a (c) D ~65 um, n1 ~1.9, and (d) D ~55 um, n1 ~2.1 sphere. Conventional microscopy cannot resolve the BD structure. Reproduced with permission from Ref. [41].

Fig. 4. Microsphere-coupled SLCM (mSLCM) under the reflection illumination mode: (a) Schematic of the experimental configuration, (b) Optical path of the mSLCM. Images of gold quintuplet nanodots on a glass substrate by (c) SEM, (d) standard SLCM, and (e) 5 um diameter Fused Silica mSLCM, where the inset is the corresponding pseudocolor image. Reproduced with permission from Ref. [42].

Fig. 5. (a) Schematic of the epi-CARS microscope. MO-W: water immersion objective; DM: 650 nm short-pass dichroic mirror; BPF: 650/60 nm band-pass filter; FL: focusing lens; PMT: Photomultiplier tube. E-CARS images of the sample (at Raman shift 2840 cm^{-1}) with spheres of diameters in the range 1-4 um on the surface: (b) at z=0 um (on the surface of the sample), (c) z=+4 um (below the surface of the sample). Intensity profiles along the line indicated by letters A and B are shown in (d). z is the focal plane position relative to the sample layer. Reproduced with permission from Ref. [30].

Fig. 6. Super-resolution fluorescent imaging by a microsphere. Comparison of conventional microscopy and use of a microsphere for fluorescent imaging of micro-/nano-particles: 1 um fluorescent particles imaged by (a) conventional microscopy and (b) using a microsphere showing a magnification 5.4X. Fluorescent particles (~100 nm) imaged by (c) conventional microscopy,

showing that these nanoparticles cannot be resolved, and (d) using a microsphere, showing that these nanoparticles can be resolved. Reproduced with permission from Ref. [27].

Fig. 7. (a) Simulation geometry for photonic nanojet generation using COMSOL: FLB - focused light beam, n0 - refractive index of the medium (*i.e.*, water), n1 - refractive index of microsphere, D - sphere diameter, Fp - focal length, Wp - full width at half maximum, Lp - length of photonic nanojet.

Fig. 8. Numerical simulation of Gaussian foci and photonic nanojets using COMSOL: Gaussian beam foci for (a) $\lambda 1$ = 532 nm, D = 5 um, NA = 1.0, (c) $\lambda 2$ = 850 nm, D = 10 um, NA = 0.7, (e) $\lambda 3$ = 1064 nm, D = 15 um, NA = 0.5, photonic nanojets for (b) $\lambda 1$ = 532 nm, D = 5 um, NA = 1.0, n2 = 1.6, (d) $\lambda 2$ = 850 nm, D = 10 um, NA = 0.7, n2 = 2.2, (f) $\lambda 3$ = 1064 nm, D = 15 um, NA = 0.5, n2 = 2.2, (g) normalized line scan profiles along the lines A and B indicated on Figs. 8(e) and 8(f), respectively. Comsol simulations were carried out in 30 um X 60 um area, but for a better view of the focused region a 10 um X 15 um area around the focus is shown here. Reproduced with permission from Ref. [24].

Fig. 9. Super-resolution photoacoustic microscope images of two square (side length 1 um) targets separated by distance 200 nm using k-wave: (a) Schematic diagram of the two-dimensional simulation geometry for photoacoustic microscopy imaging using k-wave toolbox in MATLAB, k-wave simulation of PAM B-scan images of two square (size 1 um) targets separated by a gap of 200 nm: (b) B-scan image with photonic nanojet [shown in Fig. 8(d)] excitation. (c) Normalized

line scan profile along the dotted line indicated on (b). Reproduced with permission from Ref. [24].

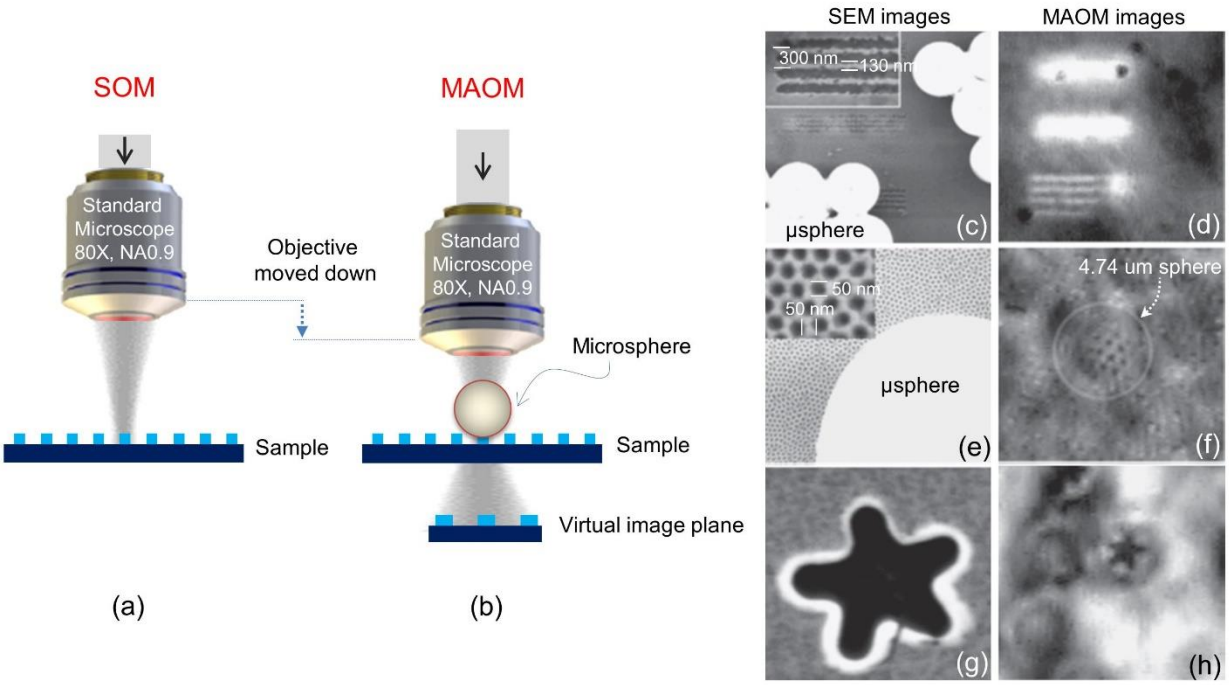

Fig. 1. Schematic of the (a) standard optical microscope (SOM), (b) microsphere-aided optical microscope (MAOM). In MAOM, the objective needs to be moved towards the sample to capture the virtual image. The sphere forms virtual images that can be captured by the standard microscope. Microsphere imaging in transmission mode: (c) SEM image of 360-nm-wide lines spaced 130 nm apart, (d) the corresponding MAOM image shows that the lines are clearly resolved. (e) SEM image of a gold-coated AAO sample. (f) The MAOM clearly resolves the pores that are 50 nm in diameter and spaced 50 nm apart. The size of the optical image between the pores within the image plane is 400 nm. It corresponds to a magnification of 8 X. Microsphere imaging in reflection mode: (g) SEM image of a star structure made on GeSbTe thin film, (h) the complex shape of the star including 90 nm corner was clearly imaged using MAOM. A SiO2 sphere with diameter 4.74 um is used for imaging. Reproduced with permission from Ref. [20].

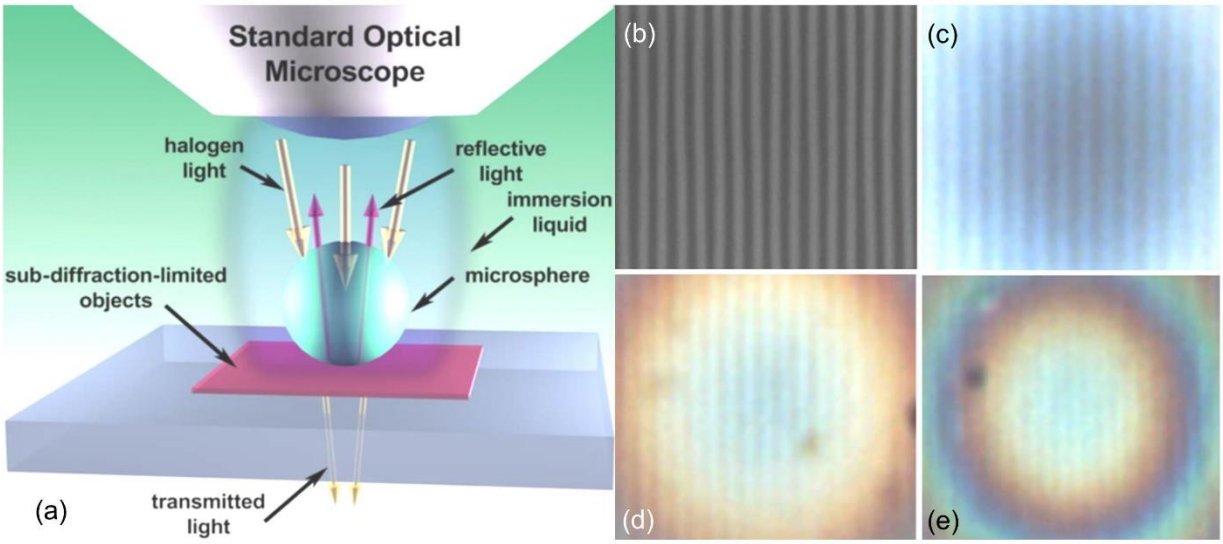

Fig. 2. Schematic of the microsphere optical nanoscopy in the reflective mode. (b) Scanning electron microscope (SEM) image of a film with a line width of 120 nm and a spacing of 180 nm. The magnified images through the MAOM in (b) water, (c) 40% sugar solution, and (d) microscope immersion oil using a 100 um diameter BaTiO3 microsphere. Reproduced with permission from Ref. [40].

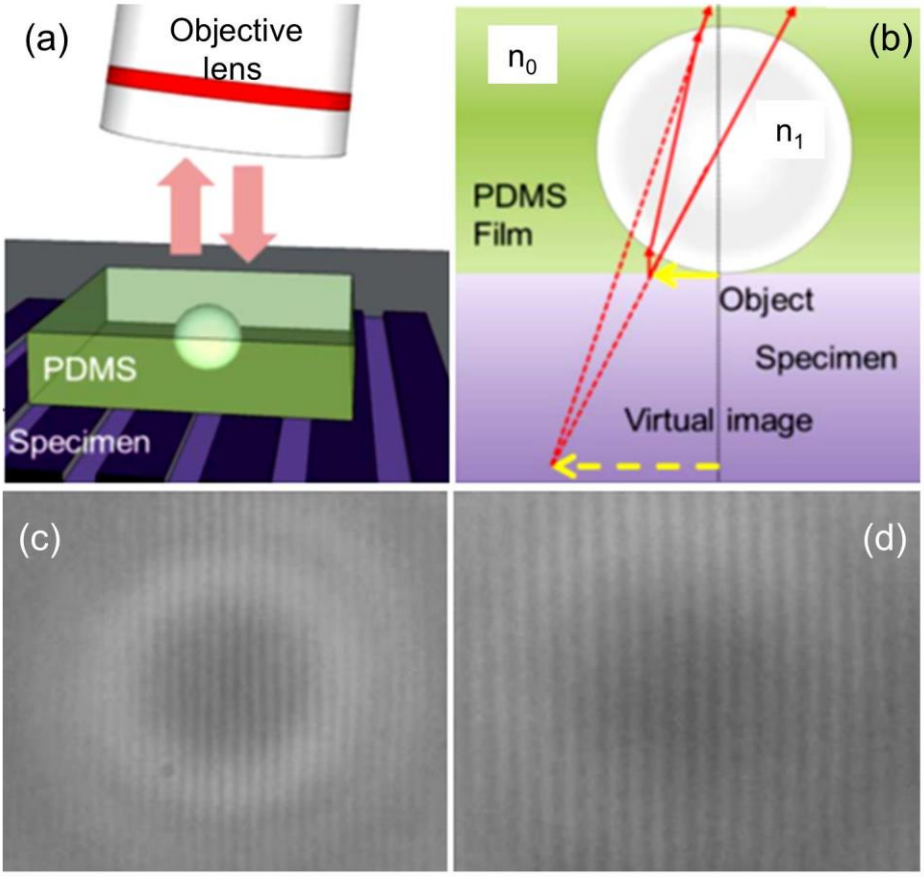

Fig. 3. Schematic of the microsphere-assisted imaging setup in which a microsphere embedded in a PDMS film: (b) ray diagram for the virtual image formation by the sphere. The structure consisting of 200-nm stripes separated by 100-nm gaps is resolved by using the microsphere-embedded film through a (c) D ~65 um, n1 ~1.9, and (d) D ~55 um, n1 ~2.1 sphere. Conventional microscopy cannot resolve the BD structure. Reproduced with permission from Ref. [41].

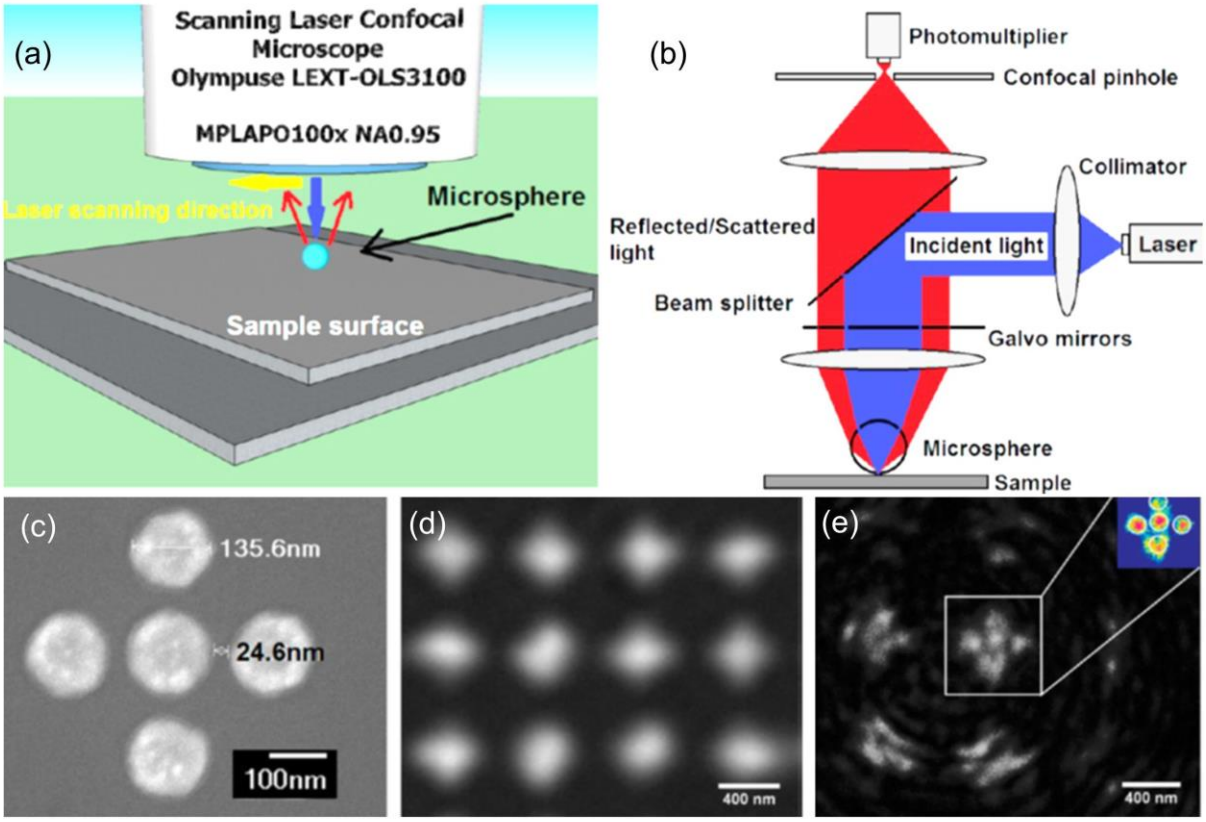

Fig. 4. Microsphere-coupled SLCM (mSLCM) under the reflection illumination mode: (a) Schematic of the experimental configuration, (b) Optical path of the mSLCM. Images of gold quintuplet nanodots on a glass substrate by (c) SEM, (d) standard SLCM, and (e) 5 um diameter Fused Silica mSLCM, where the inset is the corresponding pseudocolor image. Reproduced with permission from Ref. [42].

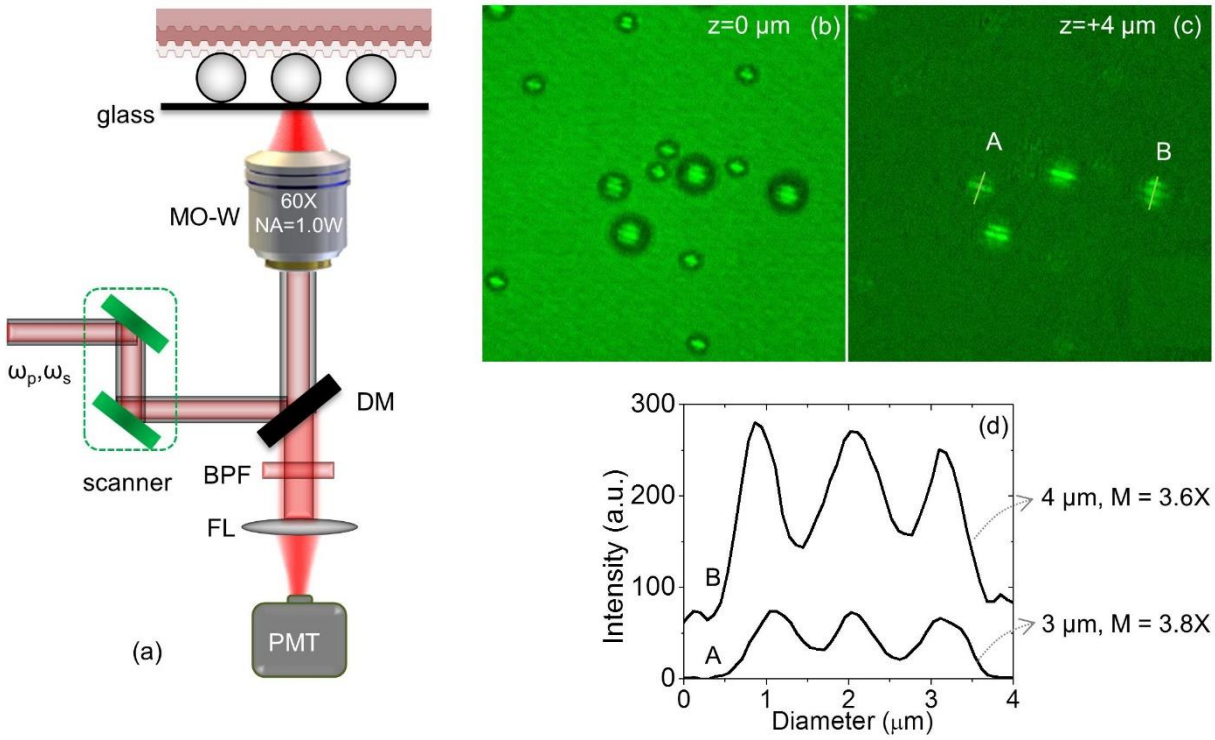

Fig. 5. (a) Schematic of the epi-CARS microscope. MO-W: water immersion objective; DM: 650 nm short-pass dichroic mirror; BPF: 650/60 nm band-pass filter; FL: focusing lens; PMT: Photomultiplier tube. E-CARS images of the sample (at Raman shift 2840 cm^{-1}) with spheres of diameters in the range 1-4 um on the surface: (b) at z=0 µm (on the surface of the sample), (c) z=+4 µm (below the surface of the sample). Intensity profiles along the line indicated by letters A and B are shown in (d). z is the focal plane position relative to the sample layer. Reproduced with permission from Ref. [30].

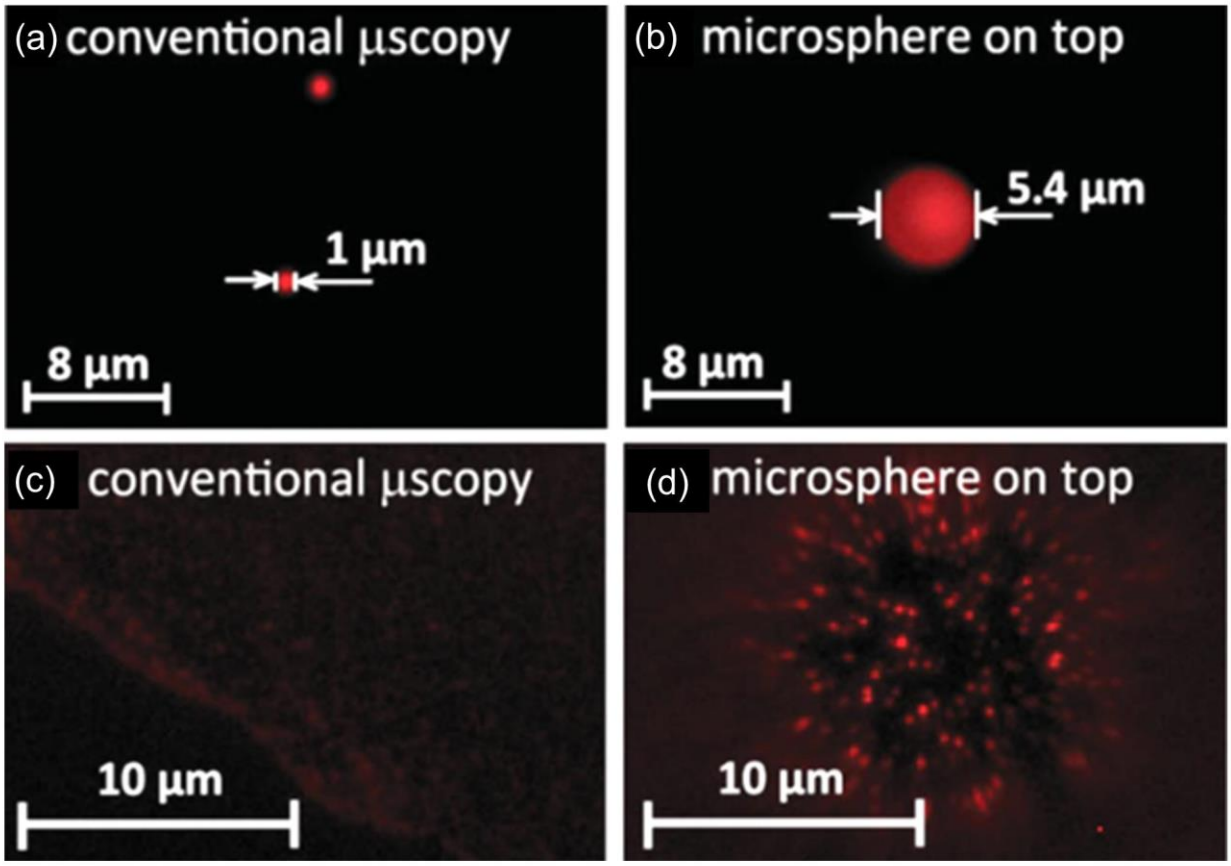

Fig. 6. Super-resolution fluorescent imaging by a microsphere. Comparison of conventional microscopy and use of a microsphere for fluorescent imaging of micro-/nano-particles: 1 μm fluorescent particles imaged by (a) conventional microscopy and (b) using a microsphere showing a magnification 5.4X. Fluorescent particles (~100 nm) imaged by (c) conventional microscopy, showing that these nanoparticles cannot be resolved, and (d) using a microsphere, showing that these nanoparticles can be resolved. Reproduced with permission from Ref. [27].

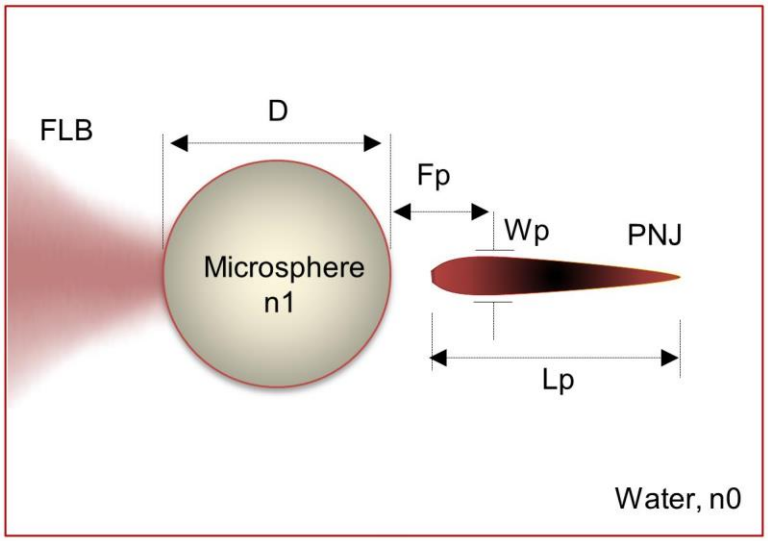

Fig. 7. (a) Simulation geometry for photonic nanojet generation using COMSOL: FLB - focused light beam, n0 - refractive index of the medium (*i.e.*, water), n1 - refractive index of microsphere, D - sphere diameter, Fp - focal length, Wp - full width at half maximum, Lp - length of photonic nanojet.

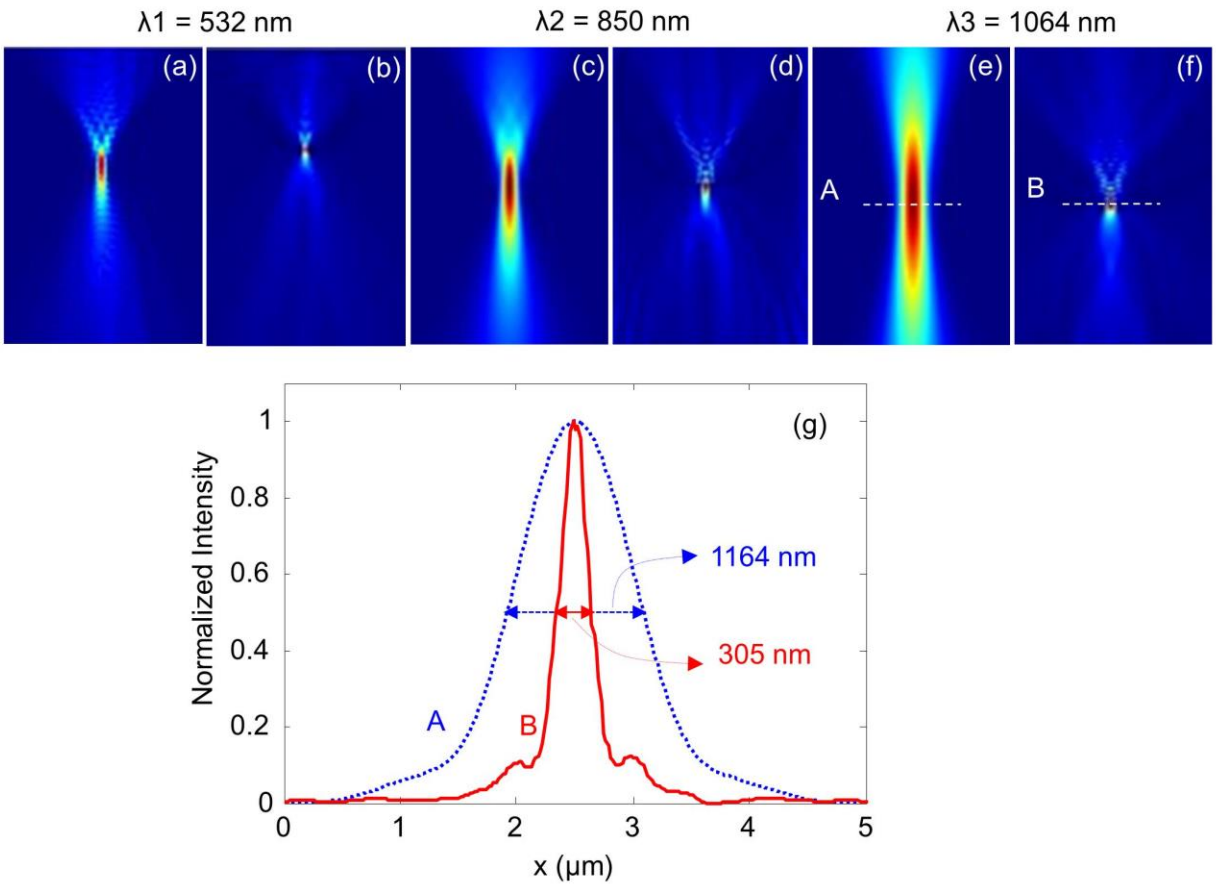

Fig. 8. Numerical simulation of Gaussian foci and photonic nanojets using COMSOL: Gaussian beam foci for (a) λ1 = 532 nm, D = 5 um, NA = 1.0, (c) λ2 = 850 nm, D = 10 um, NA = 0.7, (e) λ3 = 1064 nm, D = 15 um, NA = 0.5, photonic nanojets for (b) λ1 = 532 nm, D = 5 um, NA = 1.0, n2 = 1.6, (d) λ2 = 850 nm, D = 10 um, NA = 0.7, n2 = 2.2, (f) λ3 = 1064 nm, D = 15 um, NA = 0.5, n2 = 2.2, (g) normalized line scan profiles along the lines A and B indicated on Figs. 8(e) and 8(f), respectively. Comsol simulations were carried out in 30 um X 60 um area, but for a better view of the focused region a 10 um X 15 um area around the focus is shown here. Reproduced with permission from Ref. [24].

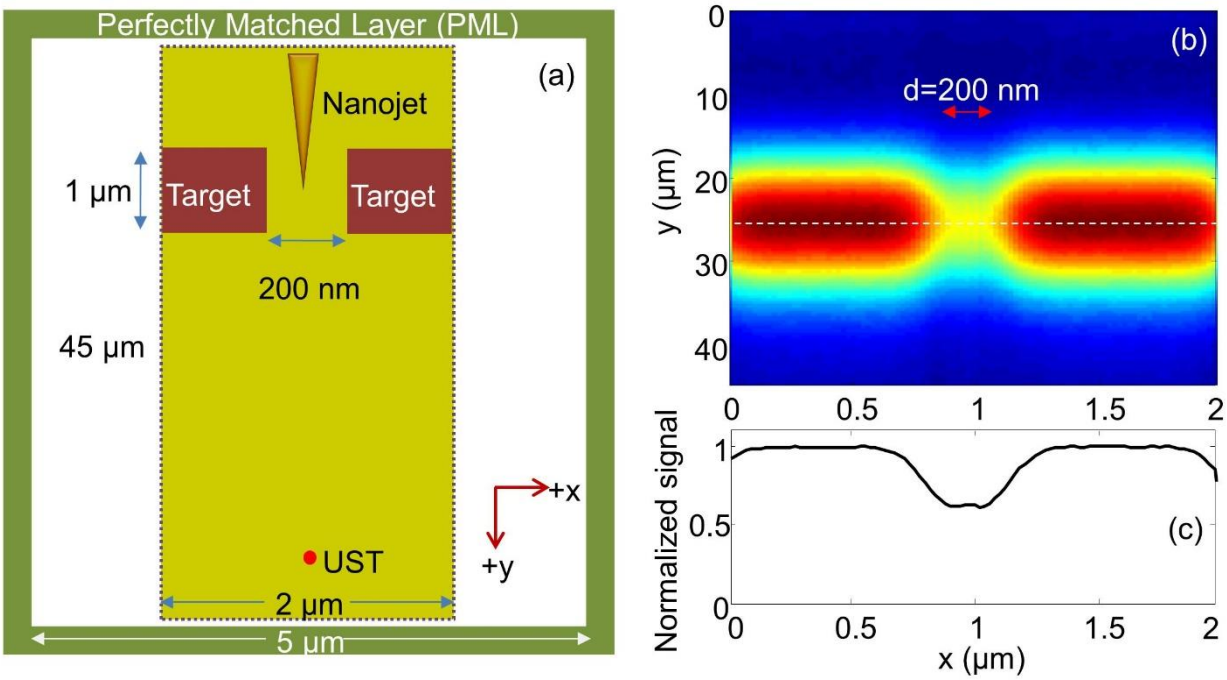

Fig. 9. Super-resolution photoacoustic microscope images of two square (side length 1 um) targets separated by distance 200 nm using k-wave: (a) Schematic diagram of the two-dimensional simulation geometry for photoacoustic microscopy imaging using k-wave toolbox in MATLAB, k-wave simulation of PAM B-scan images of two square (size 1 um) targets separated by a gap of 200 nm: (b) B-scan image with photonic nanojet [shown in Fig. 8(d)] excitation. (c) Normalized line scan profile along the dotted line indicated on (b). Reproduced with permission from Ref. [24].